13,01

Effect of Barrier Layer Roughness on the Formation of Nanoparticles of the Carbon Nanotube Growth Catalyst

© S.V. Bulyarsky, A.A. Dudin, K.I. Litvinova¶, A.A. Pavlov, G.A. Rugakov

Institute of Nanotechnology of Microelectronics, Russian Academy of Sciences, Moscow, Russia

¶ E-mail: litkristy@gmail.com

Received December 6, 2022
Revised December 6, 2022
Accepted December 10, 2022

This article compares TiN layers produced by electron beam evaporation (EBE) and atomic layer deposition (ALD) for the effect of barrier layer deposition technology on the formation of carbon nanotube (CNT) growth catalyst nanoparticles. The layers obtained by EBE have a roughness 1.5 times higher than the layers deposited by the ALD method ($R_a = 1$ nm and $R_a = 0.6$ nm). Nanoparticles formed on the surface of the EBE layer are characterized by a large average size (about 30 nm) and a 1.3 times greater dispersion of the distribution compared to nanoparticles formed on the ALD layer. TiN layers obtained by EBE are characterized by better surface wettability in comparison with ALD layers. The contact angle for catalyst nanoparticles on the surface of the EBE layer of TiN is about 30 degrees and approaches 90 degrees for ALD layers. Catalyst spreading is due to the Wenzel model. It is shown that the higher surface roughness of the EBE samples is associated with the crystallization of TiN, since the layer formation process proceeds at a higher temperature compared to the ALD process. For this reason, the use of barrier layers obtained by the ALD method is preferable for the formation of CNT growth catalyst nanoparticles on their surface.

Keywords: electron beam evaporation, atomic layer deposition, roughness, wetting, catalyst nanoparticles.

DOI: 10.21883/PSS.2023.03.55593.545

1. Introduction

Carbon nanotubes (CNTs) are widely used in micro- and nanoelectronics [1]. The growth of vertical arrays of carbon nanotubes on substrates by the Chemical Vapor Deposition (CVD) method occurs with the participation of catalysts, usually deposited on barrier layers [2,3]. The results of numerous studies have established [4] that the morphology, diameter and growth rate of carbon nanotubes are determined by the catalyst [5,6]. To fabricate a nanoelectronic element, an ensemble of catalyst nanoparticles uniform in size and density is required. This is required for the growth of a high-quality vertical array of CNT. The most commonly used catalysts for the growth of carbon nanotubes are transition metals: iron, cobalt, and nickel [6–9].

The disadvantage of these metals is the high activity with the silicon surface, consisting in diffusion with the formation of silicides, which adversely affects the catalytic properties. To prevent this, a barrier layer is added between the silicon and the catalyst metal. Titanium, tantalum or niobium nitrides are often used as barrier layers, becausethey have conductive properties and weakly interact with catalyst metals [10]. Nanoparticles are formed from nanodrops of a melted thin catalyst film $2-4$ nm thick deposited on the surface of the barrier layer. To explain the kinetics of the formation of such nanodroplets, a hydrodynamic model is proposed that reveals the role of the interaction of the catalyst with the substrate [11]. The main parameter of this model is the interaction potential of the catalyst nanodroplet with the substrate, which determines the size distribution of the catalyst nanoparticles.

Various surface preparation methods are used to order the size distributions of catalyst nanoparticles. Growth of nanotubes on porous surfaces [12–14] has been studied in a series of papers. The creation of artificial porosity leads to the achievement of a result, namely, a decrease in the dispersion of the catalyst size distribution. However, this increases the resistance of the substrate with the barrier layer, which has a negative effect on the electrical properties of the structure. Attention should be paid to other ways of preparing the substrate, including surface treatment that prevents it from being wetted by the molten catalyst metal [15]. In this case, the catalyst nanoparticles have a shape that is close to spherical, and coalescence is difficult. This contributes to a decrease in the size and dispersion of the size distribution of nanoparticles and, as is known, to the growth of thinner nanotubes.

It is known that roughness contributes to the wetting of the surface by molten metal, which causes spreading of the catalyst nanoparticle and increases the role of the coalescence process with the formation of particles of large diameter [16,17]. The purpose of this work is to study the effect of the technology of creating a barrier layer on the surface roughness and size distribution of catalyst nanoparticles. In the pursuit of this purpose, conductive

Surface roughness values of TiN layers obtained by different methods

	TiN(A)			TiN(B)		
	R_a, nm	R_q, nm	R_z, nm	R_a, nm	R_q, nm	R_z, nm
After deposition	1.01	1.22	9.70	0.58	0.74	7.46
After annealing	0.91	1.16	12.95	0.83	1.04	9.28

layers of titanium nitride are studied, obtained by various technological methods and differing in roughness.

2. Experimental part

Titanium nitride films were deposited by two different methods: electron beam evaporation (EBE) and atomic layer deposition (ALD). KEF-4.5 (100) silicon wafers were used as substrates for film deposition. Before deposition, the substrates were washed in an ammonium peroxide solution and treated in an aqueous HF solution.

Samples of titanium nitride TiN(A) (EBE process) were deposited on the substrate by the electron beam evaporation method. The wafers were mounted on a rotating substrate holder and heated for 10 min. at a temperature of 100°C to degas water vapor from the surface. Before the start of the deposition process, the residual pressure in the vacuum chamber did not exceed $5.0 \cdot 10^{-5}$ Pa. As a source, a titanium sample (purity 99.995%) was used, filled into a graphite crucible with a diameter of 20 and a height of 10 mm, and installed perpendicular to the wafer at a height of 45 cm from the wafer. The deposition process began with preliminary cleaning of the wafer surface with an argon ion beam (150 eV) with an ion current density of 100 mA for 3 min. During preliminary treatment and subsequent stages of deposition, the substrate holder with the wafer rotated at a speed of 10 rpm. The evaporation interval began with preliminary heating of the material in the crucible and stabilization of the electron beam current for 1 min. Then, the N_2 flow (purity 99.999%, flow rate 10 sccm) was introduced into the chamber and the partial pressure was stabilized at the level of 0.007 Pa. During the stabilization of the process, TiN was deposited on a closed damper located between the crucible and the substrate. The film thickness was controlled by a quartz sensor, the deposition rate was 2.3–2.4 Å/s.

TiN(B) samples (APAT process) were obtained by atomic layer deposition. Reactive gases (N_2, H_2, purity 99.999%) are introduced into the reactor from above and activated in an inductively coupled plasma source (ICP), which is separated from the main chamber valve. The ICP plasma discharge is excited by a high-frequency (HF) generator with a frequency of 13.56 MHz and a power of up to 300 W. The organometallic precursor TDMAT ($Ti(N(CH_3)_2)_4$, Sigma-Aldrich, purity 99.999%) in carrier gas Ar (purity 99.999%, flow rate 200 sccm) was used as a source of Ti. To ensure the operating pressure of saturated vapors, the TDMAT source was maintained at a temperature of 60°C, and the supply line at a temperature of 100°C in order to prevent vapor condensation on the surface of the pipelines. The APAT cycle consists of the following main steps: 0.8 s of exposure to the precursor at a pressure of 5.3 Pa; 3 s purge with argon; 2 s stabilization of pressure and flow rates of reactive gases; 3 s of a plasma discharge at a power of 300 W and a pressure of 2 Pa; 2 s purge with argon. The growth rate at a temperature of 300°C is approximately 0.09 nm/cycle.

Nickel films were deposited on the TiN(A) and TiN(B) layers in one process by the electron beam evaporation method described above. The substrate temperature and stripping time correspond to the TiN deposition process. The resulting samples were annealed at a temperature of 750°C for 5 min. in a capacitively coupled plasma discharge 13.56 MHz in a mixture of H_2/Ar (ratio 1 : 1) at a power of 50 W and a pressure of 200 Pa. During this process, the nickel film melted and the catalyst nanoparticle was formed. In order to ensure correlation between the sizes of the melt nanodroplets and nanoparticles, due to the inertia of the heating and cooling processes, the substrate was placed on a table preheated to the annealing temperature. At the end of the annealing time, the wafer was moved to a massive holder, which ensured rapid heat removal and cooling.

3. Results and discussion

3.1. Study of the TiN surface by atomic-force microscopy

Atomic-force microscopy (AFM) was used to study the surface morphology of TiN barrier layers immediately after deposition and after annealing. The surface of the layers was scanned over two areas 1×1 mkm and 5×5 mkm. A large scan area was used for statistical analysis of surface roughness. The table shows the roughness parameters: the arithmetic mean of the absolute values of the profile deviations within the base length (R_a), the root mean square of the absolute values of the profile deviations within the base length (R_q) and the difference between the largest minimum and the largest maximum (R_z).

TiN(B) layers have lower roughness compared to TiN(A) layers. Annealing of TiN layers increases the roughness within 1–3 nm. The large roughness of TiN(A) agrees with the results obtained by the TEM method and indicates

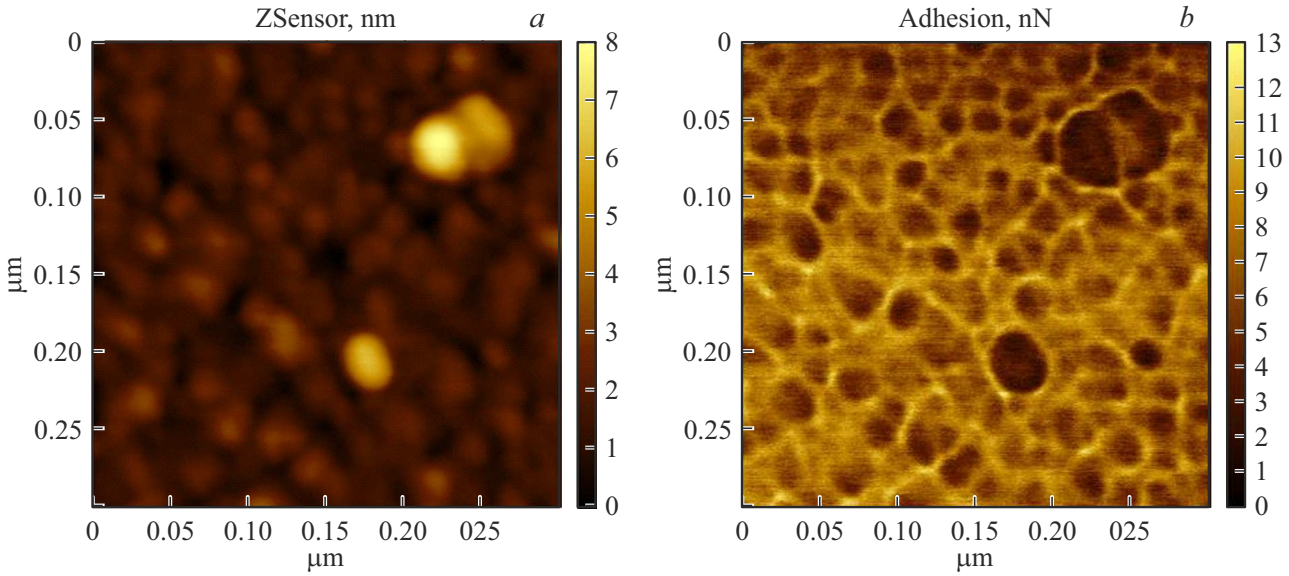

Figure 1. Distribution map of the Ni (a) nanoparticle height and adhesion force to the AFM (b)probe measured on a TiN(B) sample after annealing.

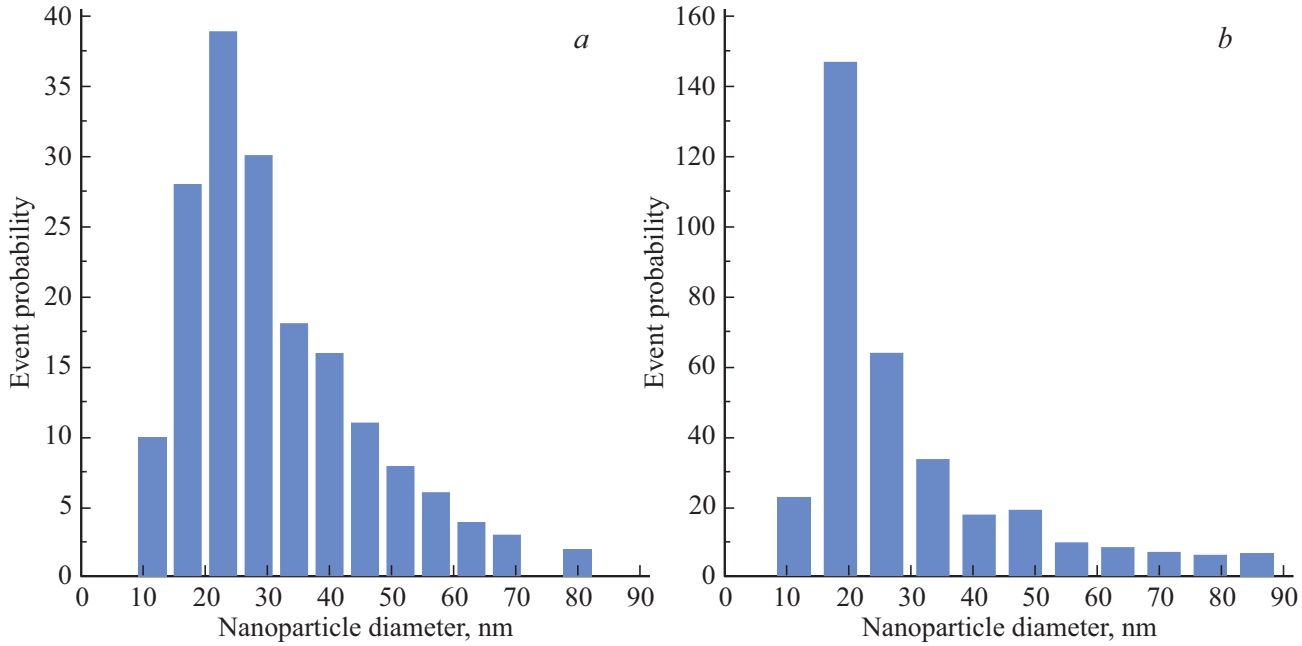

Figure 2. Size distribution of catalyst nanoparticles for TiN(A) (a) and TiN(B) (b).

heterogeneous crystallization of the films during growth and subsequent annealing. Figure 1 shows the distribution maps of the height and adhesion force to the AFM probe for TiN/Ni after annealing. The distribution of the adhesion force to the probe makes it possible to qualitatively visualize the presence of Ni nanoparticles on the surface of the TiN layer.

Based on the results obtained using AFM, the diameter distributions of Ni catalyst nanoparticles were plotted (Fig. 2). Based on the obtained distributions, the mean value of the diameter (d_m) and the variance (σ) were determined using the formulas

$$d_m = \sum_i d_i v_i, \tag{1}$$

$$\sigma = \sqrt{\sum_i (d_i - d_m)^2}, \tag{2}$$

where d_i — is the current value of the nanoparticle diameter; v_i is the expectation of this value.

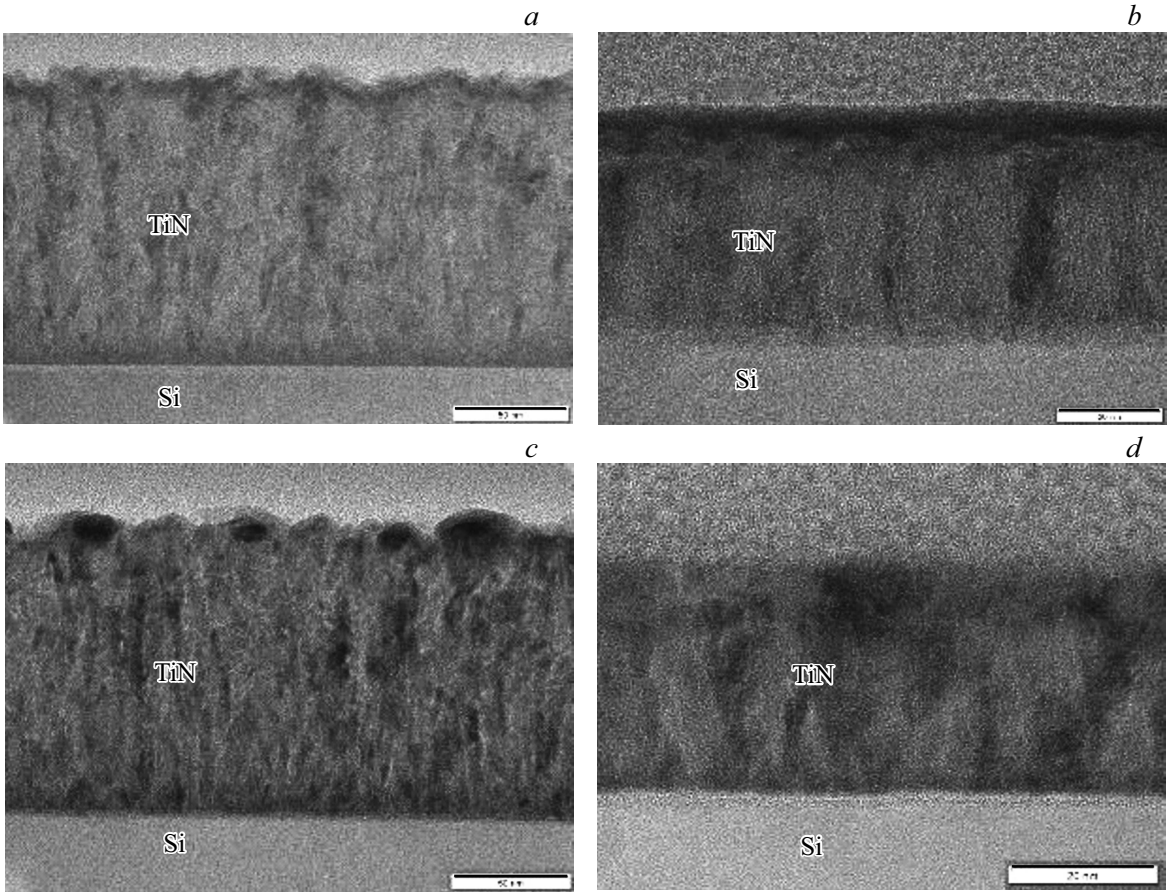

Figure 3. High resolution image of TiN(A) (a, c) and TiN(B) (b, d) samples after deposition (a, b) and after annealing (c, d).

The expectation was calculated by normalizing the results shown in Fig. 2 according to the condition $\sum_i v_i = 1$. For TiN(A) samples, the average value of the diameter is $d_m = 30.4$ nm, and the dispersion is $\sigma = 13.8$ nm; for TiN(B) samples, these quantities take the values $d_m = 25.2$ nm, and the dispersion $\sigma = 10.5$ nm.

It can be seen that an increase in surface roughness contributes to an increase in the average diameter of a catalyst nanoparticle and an increase in the dispersion of the distribution of nanoparticles over the diameter.

3.2. Transmission electron microscopy

Samples of TiN layers without and with catalyst nanoparticles formed during annealing were studied by high-resolution transmission electron microscopy (TEM) (Fig. 3). It can be seen that the initial TiN(A) titanium nitride layer has a more developed surface relief compared to the TiN(B) layer. The protrusions on the layer surface are formed by elongated nanocrystalline inclusions, which are oriented perpendicular to the substrate (Fig. 3, *a, b*). During annealing, the titanium nitride layer recrystallizes and these inclusions increase in size (Fig. 3, *c, d*). For a TiN(A) sample immediately after synthesis, the length of nanocrystalline inclusions is from 20 to 38 nm, and the width is from 7 to 9 nm. After annealing, their length increases and becomes equal to from 32 to 78 nm at the same width. Annealing increases the length of inclusions by a factor of 1.5, which seems to be the reason for the increase in surface roughness. Similar inclusions and changes are also present in the TiN(B) samples, but their sizes are smaller.

Thus, during the annealing process, which forms catalyst nanoparticles, changes occur not only in the nickel layer, but also in the TiN barrier layer. During annealing, the size of nanocrystalline inclusions in the titanium nitride layer increases. The heterogeneity of the TiN layer obtained by electron beam evaporation and the existence of nanocrystalline inclusions in it explains the graininess of the surface of this material.

The TEM-image of Ni catalyst nanoparticles on the surface of the TiN barrier layer of the TiN(A) sample is shown in Fig. 4. It can be seen that, firstly, -nickel wets the TiN surface and spreads over this surface (Fig. 4, *a*). Secondly, the catalyst nanoparticle consists of nickel nanocrystals, as evidenced by clear reflections in the electron diffraction patterns from individual sections of the catalyst (Fig. 4, *b*, 4, *c*). Thus, during annealing, the continuous catalyst film is separated into individual nanoparticles. In case of

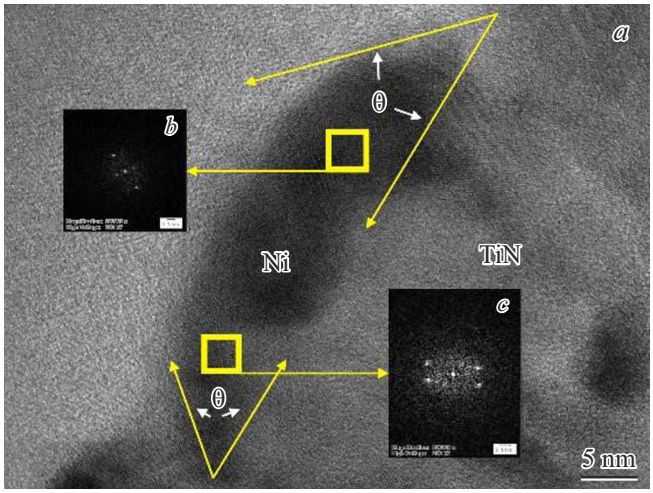

Figure 4. High resolution image of a catalyst nanoparticle on a TiN surface with local electron diffraction patterns. Sample of TiN(A).

samples obtained by electron-beam evaporation of TiN(A), this separation is not complete. It can be assumed that the small wetting angle of the TiN(A) barrier layer with nickel contributes to the occurrence of the coalescence phenomenon, when small particles, moving along the surface, merge into one particle, but of large sizes. The nickel melt wets the TiN(A) barrier layer and possibly interacts with it.

TEM-images of Ni catalyst nanoparticles of TiN(B) samples, which were synthesized by atomic layer deposition, are shown in Fig. 5. Nickel nanoparticles on the TiN(B) barrier layer have a distinct shape (Fig. 5, *a*). The contact angle increases in comparison with this angle TiN(A) and approaches 90° (Fig. 5, *b*). Therefore, the spreading of the molten catalyst droplets is less than in the previous case. Mapping in secondary electrons showed that the catalyst nanoparticles consist of nickel, which clearly stands out on the titanium nitride layer (Fig. 5, *c*, 5, *d*).

Experimental results show that the state of the surface of the barrier layer depends on the method of its synthesis.

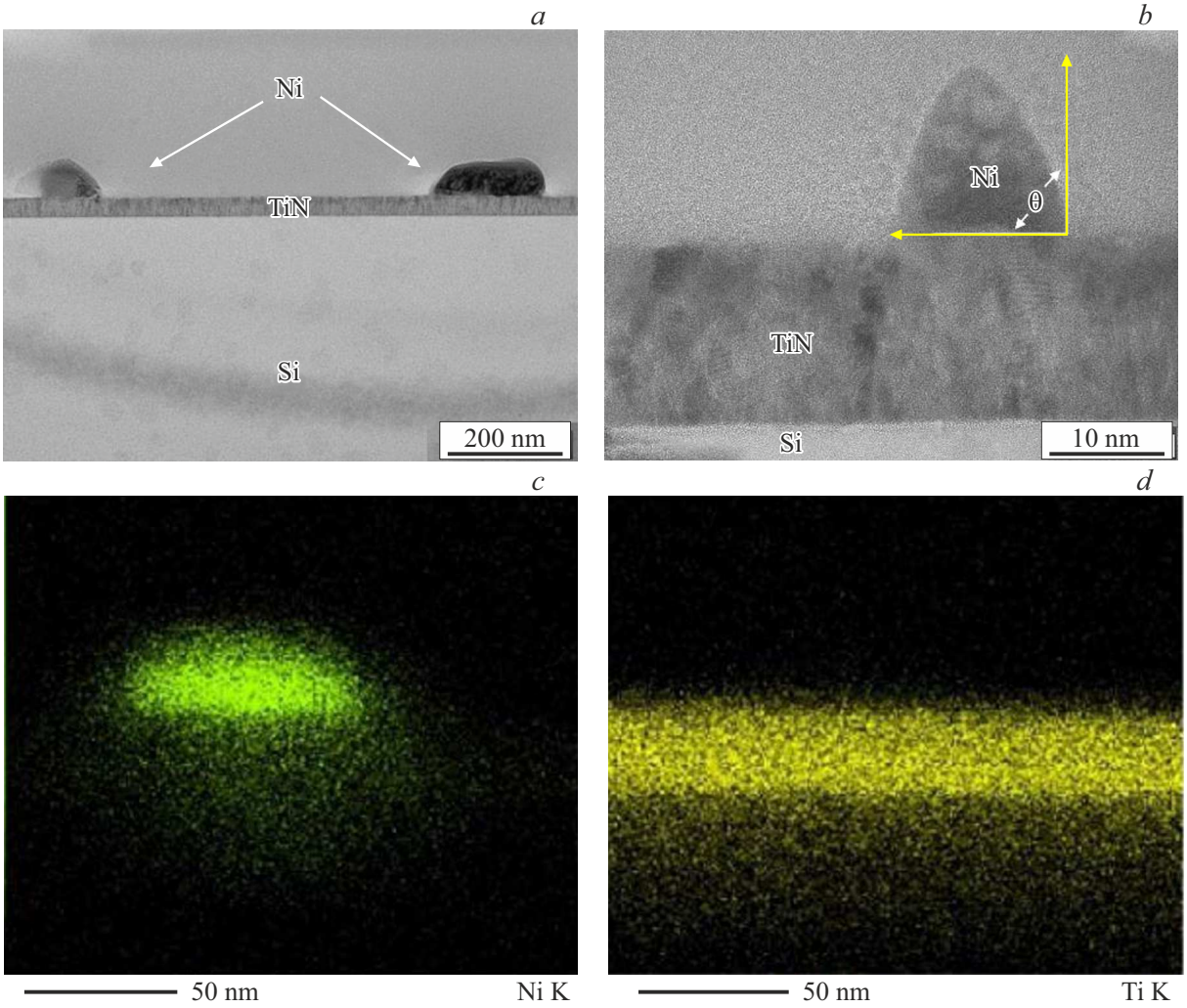

Figure 5. TEM-images of catalyst nanoparticles on the surface of a barrier layer synthesized by TiN(B) atomic layer deposition. TEM-image of a catalyst nanoparticle at different magnifications (*a*, *b*) and mapping of nickel and titanium (*c*, *d*).

The crucible containing titanium can get a high temperature during electron-beam heating [18]. Therefore, the metal atoms that fly out of the crucible have a high energy. This energy is transferred to the growing TiN film; it heats up, which promotes the growth of polycrystalline columnar formations. These inclusions lead to the development of surface roughness, the dimensions of which are larger than those of films obtained by atomic layer deposition.

The formation of catalyst nanoparticles differs on ideal and rough surfaces. As mentioned above, the kinetics and size distribution of catalyst nanoparticles on an ideal surface is described by a hydrodynamic model [11]. Obviously, in the case of a real surface, its roughness should in a certain way affect the wetting of the surface by the molten catalyst nanodroplet. The review [19] considers various methods for obtaining developed surfaces and the effect of roughness on surface wetting. It is shown that the wetting ability is a combination of hydrophilic properties and surface roughness. Existing theoretical models explaining the effect of surface texture on wetting are complex and do not provide a simple procedure for predicting thermodynamic stable and metastable states and their corresponding wetting angles [20]. Experimental studies show that metal melts, as a rule, wet the surface and spread over it, as follows from the Deryagin–Wenzel theory [16,17]. Improving the wetting of rough surfaces by the metal melt and reducing the contact angle depends on the geometric shape of the texture elements, depressions and irregularities that characterize such a surface [21]. Theoretical studies show that the melt spreading is influenced by the roughness gradient [22], which causes the metal to be drawn into the surface depression and promotes its spreading. The work [23] also found an improvement in the wetting of rough surfaces by metal melt, however, it is noted that a significant increase in roughness can lead to the opposite effect due to the fact that large surface heterogeneities create barriers and prevent the spread of the melt. This assumption is consistent with theoretical calculations showing that the application of the Wenzel theory is possible in the case when the droplet size exceeds the roughness size by approximately 40 [24]. In our case, this relation is approximately fulfilled. According to existing theories, the penetration of molten metal into surface depressions is a process similar to the penetration of a wetting liquid into capillaries when the wetting angle is $\theta < 90^\circ$. If the contact angle is $\theta > 90^\circ$, then the liquid does not penetrate into the roughness depressions. Thus, roughness increases wetting on a hydrophilic surface and decreases wetting on a hydrophobic surface. This phenomenon is described by the Wenzel–Deryagin equation [16,17]:

$$\cos\theta^r = \Delta S_q \cos\theta, \tag{3}$$

where θ^r — the contact angle of a rough surface, θ — the contact angle of a smooth surface, ΔS_q — a coefficient that shows how many times the area of a rough surface is greater than that of a smooth one.

The cosine of the wetting angle of a rough surface increases, and the angle accordingly decreases. This leads to an increase in the average particle size and an increase in the dispersion of the distribution of nanoparticles, which we observed experimentally.

4. Conclusion

Titanium nitride samples grown by TiN(A) electron beam evaporation and TiN(B) atomic layer deposition differ in the level of roughness (table). The roughness is about one and a half times greater in the first case than in the second. The formation of catalyst nanoparticles occurs during the melting of its film with a thickness of (2–4) nm. The result of formation is affected by the interaction of the catalyst with the substrate. This interaction for an ideally smooth substrate is determined by the interaction potential, which determines the kinetics of the formation of nanoparticles and their size distribution [11]. For a non-ideal rough surface, an additional contribution to the spreading of the catalyst nanodroplet is made by the Wenzel mechanism, in which the melt fills the roughness, which, when this surface is wetted, leads to an additional spreading of the melt [16,17]. The present work shows that an increase in roughness leads to a decrease in the contact angle, which is confirmed by the data of transmission electron microscopy. Therefore, the average size of nickel nanoparticles on the surface of the TiN barrier layer increases, and the dispersion of the distribution of nanoparticles over their diameter increases, since increased wetting stimulates the development of the coalescence phenomenon, which consists in the coalescence of small nanodroplets into large ones. This leads to an increase in average diameters and, as a consequence, an increase in the diameter of future CNT, since their diameters are proportional to each other [25]. Thus, for the formation of catalyst nanoparticles, it is desirable to choose the most smooth surfaces that are not wetted by the catalyst melt. This contributes to a decrease in the dispersion of the size distribution of nanoparticles, which has a positive effect on the homogeneity of CNT arrays.

Funding

The work was supported by the Russian Ministry of Education and Science, project No. 0004-2022-0004, using the unique scientific unit for silicon-carbon technology of heterogeneous integration at the Institute of Nanotechnology of Microelectronics of the Russian Academy of Sciences.

Acknowledgments

The authors would like to thank: M.I. Krasilnikov, M.S. Molodensky — sample preparation; T.S. Grishin — ASM-research; E.M. Eganova, E.A. Pershina — TEM-research.

Conflict of interest

The authors declare that they have no conflicts of interest.

References

[1] J. Liu, D. Jiang, Y. Fu, T. Wang. Adv. Manuf. **1**, *1*, 13 (2013).
[2] S.V. Bulyarskiy, G.G. Gusarov, A.V. Lakalin, M.S. Molodenskiy, A.A. Pavlov, R.M. Ryazanov. Diamond Rel. Mater. **103**, 107665 (2020).
[3] S.V. Bulyarskiy, A.V. Lakalin, A.A. Pavlov, A.A. Dudin, E.P. Kitsyuk, E.M. Eganova, A.A. Shamanaev. Tech. Phys. Lett. **43**, *4*, 366 (2017).
[4] S.V. Bulyarskiy, A.S. Basaev. Catalysts for the growth of carbon nanotubes. Moscow, M. (2016). 117 p. (in Russian).
[5] A. Steplewska, E. Borowiak-Palen. J. Nanopart. Res. **13**, *5*, 1987 (2011).
[6] G. Boskovic, S. Ratkovic, E. Kiss, O. Geszti. Bull. Mater. Sci. **36**, *1*, 1 (2013).
[7] S.Yu. Davydov, A.Yu. Kryukov, I.M. Izvolsky, E.G. Rakov. Neorgan. materialy **49**, *3*, 255 (2013). (in Russian).
[8] T.Y. Tsai, Y.A. Li, H.C. Su, N.H. Tai, K.C. Chen, S.H. Lee, Y.Y. Chang. Diamond Rel. Mater. **17**, *4*, 594 (2008).
[9] A.S. Abdulkareem, I. Kariim, M.T. Bankole, J.O. Tijani, T.F. Abodunrin, S.C. Olu. Arab. J. Sci. Eng. **42**, *10*, 4365 (2017).
[10] S.V. Bulyarskiy, E.V. Zenova, A.V. Lakalin, M.S. Molodenskii, A.A. Pavlov, A.M. Tagachenkov, A.V. Terent'ev. Tech. Phys. **63**, 1834 (2018).
[11] P.E. L'vov, S.V. Bulyarskiy, G.G. Gusarov, M.S. Molodenskiy, A.A. Pavlov, R.M. Ryazanov, A.A. Dudin, V.V. Svetukhin. J. Phys. Condens. Matter. **32**, *24*, 245001 (2020).
[12] J.W. Ward, B.Q. Wei, P.M. Ajayan. Chem. Phys. Lett. **376**, *5*, 717 (2003).
[13] V. Asokan, D. Velauthapillai, R. Lovlie, D.N. Madsen. J. Mater. Sci. Mater. Electron. **24**, *9*, 3231 (2013).
[14] J. Fang, I. Levchenko, Z.J. Han, S. Yick, K.K. Ostrikov. Nanoscale Res. Lett. **9**, *1*, 1 (2014).
[15] J. Chen, X. Xu, L. Zhang, S. Huang. Micro Nano Lett. **7**, *4*, 353 (2015).
[16] R.N. Wenzel. J. Phys. Chem. **53**, *9*, 1466 (1949).
[17] B.V. Deryagin, N.V. Churaev, V.M. Muller. Surface forces. Nauka, M. (1985). 398 p. (in Russian).
[18] P.E. L'vov, S.V. Bulyarskiy, A.N. Saurov, V.V. Svetukhin, A.I. Terentyev. J. Vac. Sci. Technol. B **39**, *6*, 064201 (2021).
[19] N. Mahayuddin, J.A. Wahab, M. Salleh, S.F. Roduan, H.K. Chen. J. Tribol. Int. **27**, 8 (2020).
[20] Y. Kaufman, S.-Y. Chen, H. Mishra. J. Phys. Chem. **121**, 5642 (2017).
[21] G.V. Kuznetsov, E.G. Orlova, D.V. Feoktistov, A.G. Islamova, A.V. Zhuikov. Met. Mater. Int. **26**, *1*, 46 (2020).
[22] R.G. Cox. J. Fluid Mech. **131**, *1*, 26. (1983).
[23] K.J. Kubiak, M.C.T. Wilson, T.G. Mathia, S. Carras. Scan. **33**, *5*, 370 (2011).
[24] D. Kim, N.M. Pugno, S. Ryu. Sci. Rep. **6**, *1*, 1 (2016).
[25] S.V. Bulyarskiy, E.V. Zenova, A.V. Lakalin, M.S. Molodenskii, A.A. Pavlov. Tech. Phys. **63**, *12*, 1834 (2018).

Translated by E.Potapova